Astronomy & Astrophysics

Weak evidence for variable occultation depth of 55 Cnc e with TESS

E. A. Meier Valdés(ORCID), B. M. Morris(ORCID), R. D. Wells, N. Schanche(ORCID), and B.-O. Demory(ORCID)

Center for Space and Habitability (CSH), University of Bern, Gesellschaftsstrasse 6, 3012 Bern, Switzerland
e-mail: erik.meiervaldes@csh.unibe.ch

ABSTRACT

Context. 55 Cnc e is in a 0.73 day orbit transiting a Sun-like star. It has been observed that the occultation depth of this super-Earth, with a mass of 8 $M_\oplus$ and radius of 2 $R_\oplus$, changes significantly over time at mid-infrared wavelengths. Observations with *Spitzer* measured a change in its day-side brightness temperature of 1200 K, possibly driven by volcanic activity, magnetic star-planet interaction, or the presence of a circumstellar torus of dust.
Aims. Previous evidence for the variability in occultation was in the infrared range. Here we aim to explore if the variability also exists in the optical range.
Methods. The Transiting Exoplanet Survey Satellite (TESS) observed 55 Cnc during sectors 21, 44, and 46. We carefully detrended the data and fitted a transit and occultation model for each sector in a Markov chain Monte Carlo (MCMC) routine. In a later stage, we used the leave-one-out (LOO) cross-validation statistic to compare with a model of constant occultation for the complete set and a model with no occultation.
Results. We report an occultation depth of 8 ± 2.5 ppm for the complete set of TESS observations. In particular, we measured a depth of 15 ± 4 ppm for sector 21, while for sector 44 we detected no occultation. In sector 46 we measured a weak occultation of 8 ± 5 ppm. The occultation depth varies from one sector to the next between 1.6 and 3.4 σ significance. We derived the possible contribution on reflected light and thermal emission and set an upper limit on the geometric albedo. Based on our model comparison, the presence of an occultation is favoured considerably over no occultation, and the model with varying occultation across sectors takes most of the statistical weight.
Conclusions. Our analysis confirms a detection of the occultation in TESS. Moreover, our results weakly lean towards a varying occultation depth between each sector, while the transit depth is constant across visits.

Key words. stars: individual: 55 Cnc – techniques: photometric – occultations – planets and satellites: individual: 55 Cnc e

1. Introduction

55 Cnc e was first discovered by McArthur et al. (2004) via radial velocity (RV) observations with the Hobby-Eberly Telescope (HET) in a 2.808 day orbit and was later found to be an alias of its true period of 0.7365 days (Dawson & Fabrycky 2010). Winn et al. (2011) and Demory et al. (2011a) confirmed the period and detected the planet to be transiting its host star, which is one of the brightest stars ($V = 6.0$) known to host planets.

The conundrum of 55 Cnc e's nature began with the detection of a phase modulation that was too large to be caused by reflected starlight and thermal emission of the planet (Winn et al. 2011) which was later found to vary over time (Dragomir et al. 2012; Sulis et al. 2019). Given the short separation to the star, a possible explanation is star-planet interaction. Folsom et al. (2020) derived a map of the large-scale stellar magnetic field of 55 Cnc, concluding that planet e orbits within the Alfvén surface of the stellar wind, which allows for magnetic star-planet interactions.

Demory et al. (2015) found a 300% difference in occultation depth between 2012 and 2013 in the *Spitzer*/IRAC (Werner et al. 2004; Fazio et al. 2004) 4.5 µm channel, which translates into a change in day-side brightness temperature of approximately 1200 K, later confirmed independently by Tamburo et al. (2018). This could be caused by volatile loss through surface evaporation, volcanic activity on the surface of the planet, or

the presence of an inhomogeneous circumstellar torus of dust (Demory et al. 2015; Tamburo et al. 2018; Sulis et al. 2019).

Observations over different wavelengths can shed light on the nature of a planet, providing complementary information about the planetary atmosphere. This system has already benefitted from observations in the infrared (IR) (Demory et al. 2011a, 2015, 2016; Tamburo et al. 2018), optical (Winn et al. 2011; Dragomir et al. 2012; Sulis et al. 2019; Kipping & Jansen 2020; Morris et al. 2021), far-ultraviolet, (Bourrier et al. 2018b) and X-ray (Ehrenreich et al. 2012). This list is not exhaustive. Here we present the analysis of the transit and occultation for all observations made by the Transiting Exoplanet Survey Satellite (TESS) (Ricker et al. 2014) so far.

2. Methods

2.1. TESS observations

55 Cnc e (TIC 332064670) was observed by TESS during sector 21, 44, and 46. Each sector consists of two TESS orbits. The time interval between the first set of observations and the second is approximately 600 days. The gap between the observations of sector 44 and 46 consists of 29 days. The target was not observed during sector 45. The observations include a total of 93 transits and occultations each. We use the 120-second cadence

Pre-search Data Conditioning (PDC) light curve data from the Science Processing Operations Center (SPOC) pipeline (Jenkins et al. 2016).

To prepare our data, first we removed all points above 4σ from the median of the absolute deviations. We computed a Lomb-Scargle periodogram (VanderPlas 2018, and references therein) to check for significant periodicities. Besides planet e's period and aliases, there was a strong signal between 6 and 6.5 days, corresponding to momentum dumps. To remove trends in the data, we masked all transits and occultations, then fitted a robust M-estimator using Tuckey's biweight function implemented in `wotan` (Hippke et al. 2019), setting the length of the filter window to match planet e's orbital period. After detrending, we did a second clipping to remove outliers above 4σ.

Although the PDC light curves were already corrected for background noise, stray light, and several other quality flags, we noticed flux ramps before or after momentum dumps, which often coincide with stray light reflected from Earth. Since these short-timescale events are difficult to correct without affecting astrophysical signals, we followed a similar procedure as Beatty et al. (2020) and trimmed a portion of the data preceding and following these events. In particular, we removed 1.42 days at the beginning of the first orbit in sector 21, 0.06 days at the end of the first orbit in sector 21, and 1.09 days at the beginning of the second orbit in sector 21; 0.8 days at the beginning of the first orbit in sector 44, 0.02 days at the end of the first orbit in sector 44, and 2.43 days at the beginning of the second orbit in sector 44; and 2.261 days and 2.43 days at the beginnings of both orbits in sector 46. The information regarding momentum dumps, quality flags, and a summary of each sector was obtained from the TESS data release notes[1] for each sector and the corresponding data validation files. The photon noise contribution for 55 Cnc (TESS mag = 5.2058) over a 2-hour timescale was 63.26 ppm, 57.94 ppm, and 60.69 ppm for sector 21, 44, and 46, respectively.

We also removed all flagged data points from the time series. In total, we removed 1678 of 17 319 data points for sector 21, 647 of 15247 data points for sector 44, and 4097 of 16 714 data points for sector 46. After this process, our photometric data contained 84 transits and 84 occultations.

2.2. Light curve analysis

First, we restricted the data set to 0.25 in phase before and after mid-transit to ensure we covered more than twice the transit duration (0.0648 days, Sulis et al. 2019) preceding and following the epoch of mid-transit. Keeping the transits and occultations masked, we computed the out-of-transit mean flux for each segment containing one of the 84 transits and then detrended the observations. The reasons for doing this step were to ensure a normalised out-of-transit mean flux of unity and to keep our light curve model Markov chain Monte Carlo (MCMC) with as few free parameters as possible.

The light curve model is based on those of Mandel & Agol (2002), implemented in the `exoplanet` Python package (Foreman-Mackey et al. 2021). All three sectors were analysed together. We assumed a circular orbit (Bourrier et al. 2018a) and a quadratic stellar limb-darkening law. The priors on the limb-darkening coefficients were obtained from a list (Claret 2017) of coefficients for TESS based on a 1D Kurucz ATLAS stellar atmosphere model (Castelli & Kurucz 2004). In our transit model, we fitted for the time of mid-transit, orbital period, quadratic limb-darkening coefficients, planet-to-star radius ratio,

---

[1] https://archive.stsci.edu/tess/tess_drn.html

and impact parameter. Our model was implemented in a MCMC with the PyMC3 probabilistic programming package (Salvatier et al. 2016). We fitted for a planet-to-star radius ratio for each sector, while the rest of the parameters represented a single value for all sectors. In this manner, we were able to compare the transit and occultation depth between sectors instead of obtaining a composite fit. To compute the transit depth for a given stellar limb-darkening law and impact parameter, we implemented the analytic solutions from Heller (2019) in our MCMC algorithm.

The second step consisted of freezing the best-fit parameters from the transit model (Garhart et al. 2020) for another MCMC run, fitting for the occultation depth. In this case, the limb-darkening coefficients were fixed to zero. To fit for the occultation, we considered data points before and after 0.25 in phase from the occultation centre. Here, we allowed the occultation depth parameter to explore negative values. For both the transit and occultation model MCMC, we checked that the chains are well mixed and that the Gelman-Rubin statistic is below 1.01 for all parameters (Gelman & Rubin 1992). Finally, we computed a power spectrum of the residuals to make sure that after removing the signal of the planet, there were no significant signals remaining. We also constructed an MCMC algorithm to fit a single occultation depth parameter on the complete observations and a model with the occultation depth fixed to zero.

To ensure our models are robust, after running each model, we estimated the out-of-sample predictive accuracy with leave-one-out (LOO) cross-validation (Vehtari et al. 2016) to detect any data point with a shape parameter $\hat{k}$ of the Pareto distribution greater than 0.7. Essentially, if a single point has a shape parameter greater than 0.7, the model is considered unreliable (Vehtari et al. 2015). In total, we rejected 22 points after five iterations.

3. Results

3.1. Transit depth

In Table 1, we present best-fit values. We find a transit depth consistent for all sectors within the uncertainties. Figure 1 shows a portion of the phase including the transit for each sector and the corresponding transit model overlapped. Figure A.1 in Appendix A shows the posterior distribution and correlations between all parameters sampled with our MCMC. The unbinned residual root mean square (RMS) is 166.2 ppm, 134.02 ppm, and 146.48 ppm for sector 21, 44, and 46, respectively (see Appendix B).

Based on the marginal 1.6σ difference, we conclude that there is no variability in the transit depth during the time of observation in the TESS bandpass. Compared to the observations done by the CHaracterising ExOPlanet Satellite (CHEOPS) and analysed by Morris et al. (2021), their best-fit values imply a similar transit depth of $339.72^{25.33}_{-23.54}$. Winn et al. (2011) reported a transit depth of 380 ± 52 ppm for MOST, while Tamburo et al. (2018) and Demory et al. (2015) obtained 336 ± 18 and 360 ± 26 for *Spitzer*, respectively.

3.2. Occultation depth

The occultation depths for each sector are shown in Table 1. The posterior distributions are shown in Fig. 2 and the resulting occultation light curves for each sector are shown in Fig. 3. The correlation between free parameters and the corresponding posterior distributions are shown in Fig. A.2. Our composite occultation model yields a depth of $8.11^{+2.62}_{-2.50}$ ppm, confirming a positive detection for the complete TESS data set. The

Table 1. Best-fit parameters for all sectors.

Priors	
r_{star} [$R_\odot$]	$0.943^{+0.01}_{-0.01}$
m_{star} [$M_\odot$]	$0.905^{+0.015}_{-0.015}$
Parameter	Value
P [days]	$0.73654627^{+0.00000022}_{-0.00000022}$
T_0 [BJD]	$2458870.692582^{+0.000163}_{-0.000159}$
b	$0.358^{+0.030}_{-0.033}$
u_0	$0.187^{+0.128}_{-0.113}$
u_1	$0.507^{+0.196}_{-0.214}$
$(R_p/R_s)_{21}$	$0.01708^{+0.00024}_{-0.00024}$
$(R_p/R_s)_{44}$	$0.01684^{+0.00023}_{-0.00024}$
$(R_p/R_s)_{46}$	$0.01675^{+0.00023}_{-0.00025}$
$\delta_{t,21}$ [ppm]	$337^{+8.3}_{-8.3}$
$\delta_{t,44}$ [ppm]	$328^{+8.0}_{-7.9}$
$\delta_{t,46}$ [ppm]	$324^{+7.7}_{-8.4}$
$\delta_{e,21}$ [ppm]	$15.40^{+4.11}_{-4.11}$
$\delta_{e,44}$ [ppm]	$0.25^{+4.33}_{-4.33}$
$\delta_{e,46}$ [ppm]	$7.86^{+4.57}_{-4.56}$

Notes. The priors on stellar radius r_{star} and stellar mass m_{star} are based on von Braun et al. (2011). The value presented is the median and 1σ confidence interval. The symbols stand for: P, period; T_0, BJD mid-transit time; u_0 and u_1, quadratic limb-darkening coefficients; R_p/R_s, planet-to-star radius ratio; δ_t, transit depth, and δ_e, occultation depth. The number in the subscript refers to the corresponding sector.

occultation depth of sector 21 is consistent within 1σ of the value reported by Kipping & Jansen (2020). Between sector 21 and 44, there is a significant 3.4σ decrease in the occultation and a marginal increase of 1.6σ from sector 44–46.

Our depths are considerably smaller compared to the occultation depth measured in the mid-infrared with *Spitzer* (Demory et al. 2015). During the 2012 and 2013 campaigns, they measured an occultation depth of 47 ± 21 ppm and 176 ± 26 ppm, respectively. This difference is expected due to the stronger thermal emission of planet e in the *Spitzer* bandpass than in TESS.

3.3. Reflected light and thermal emission

To put our results into perspective, we estimated the thermal contribution in the TESS bandpass. We retrieved a theoretical stellar spectrum from the PHOENIX stellar model (Husser et al. 2013) with an effective temperature of 5200 K, surface gravity $\log(g) = 4.5$ (von Braun et al. 2011), and a planet temperature of 2697 K, which is the maximum hemisphere-averaged temperature measured by Demory et al. (2016) with *Spitzer* observations. Given these values, the thermal contribution in the TESS bandpass is 10.75 ppm. Thus, the occultation depths in sector 21 and 46 are compatible with the thermal contribution within 1σ, while the depth in sector 44 is approximately 2σ below this value.

For a given occultation depth, we estimated the possible contribution of the reflected light. The geometric albedo A_g can be related to the thermal emission and reflected component as
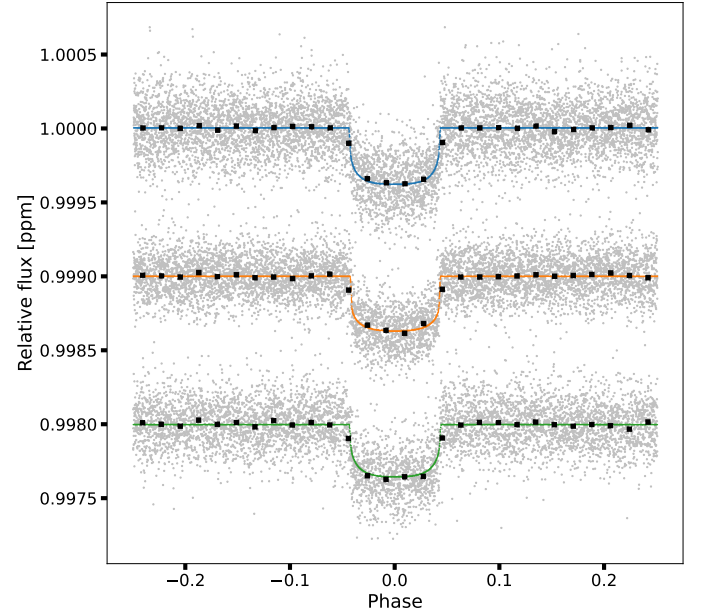

Fig. 1. Phase-folded relative flux displaying the transit. The light curves were shifted down for clarity. The top light curve corresponds to sector 21, the middle light curve to sector 44, and the bottom to sector 46. Silver points are detrended flux measurements. The continuous lines show the transit model, where sector 21 is depicted in blue, sector 44 in orange, and sector 46 in green. We keep this convention for the rest of this work. Black squares represent binned data. We note that bins are for visualization and were not used in our analysis.
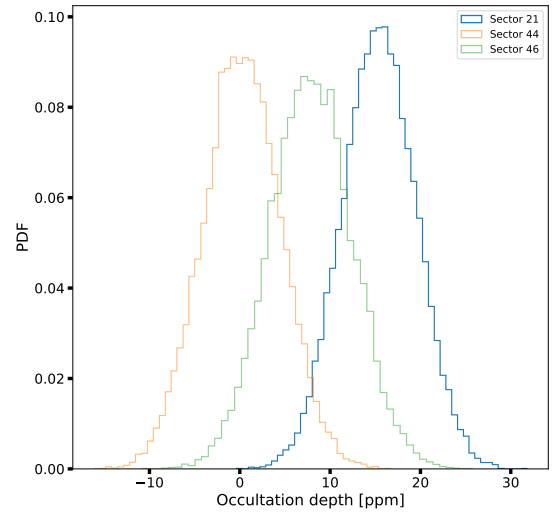

Fig. 2. Posterior density distribution functions for the occultation depth parameter in sector 21 (blue), sector 44 (orange), and sector 46 (green) in the light curve model.

(Mallonn et al. 2019)

$$A_g = \delta \left(\frac{a}{R_p}\right)^2 - \frac{B(\lambda, T_p)}{B(\lambda, T_s)} \left(\frac{a}{R_s}\right)^2, \qquad (1)$$

where d is the measured occultation depth, a is the orbital semi-major axis, R_p and R_s are the planetary and stellar radius, respectively; $B(\lambda, T_p)$ and $B(\lambda, T_s)$ are the black-body emissions of the planetary day-side and the star at temperatures T_p and T_s, respectively. Using Eq. (1) we derived the geometric albedo for a range of brightness temperatures of planetary day-side between
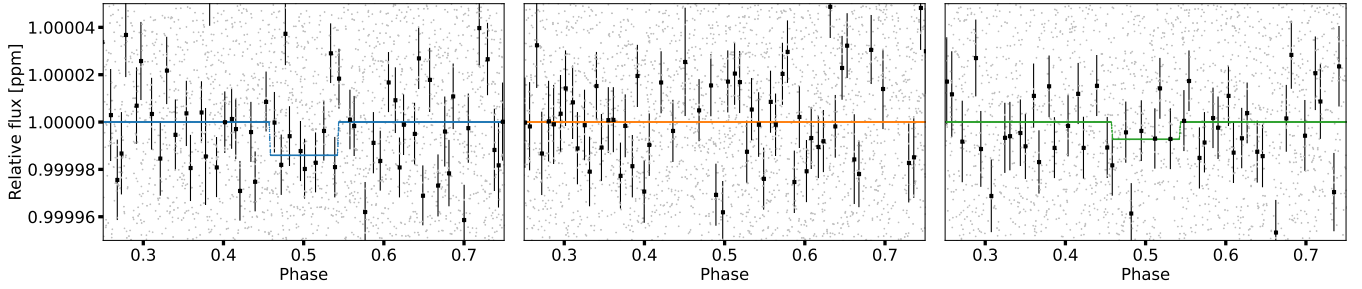
Fig. 3. Zoom on the phase-folded relative flux displaying the occultation. The silver dots are detrended flux and the black dots are binned data with their corresponding uncertainty. *Left*: detrended flux and best-fit occultation model in blue, corresponding to sector 21. *Middle*: detrended flux and best-fit occultation model in orange, corresponding to sector 44. *Right*: detrended flux and best-fit occultation model in green, corresponding to sector 46.
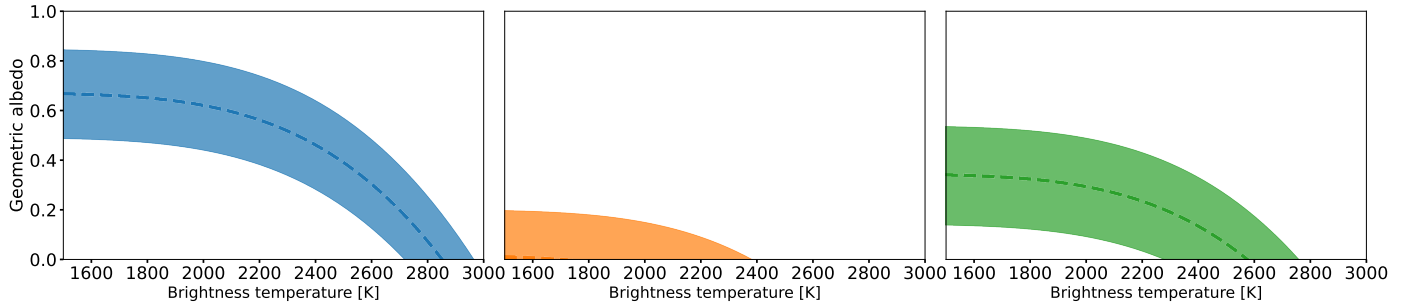

Fig. 4. Relationship between geometric albedo and brightness temperature constrained by the TESS measurements. The dashed line shows the contour for the measured occultation depth for each sector, and the shaded area represents a 1σ confidence interval based on the results in Table 1. *Left*: sector 21. *Middle*: sector 44. *Right*: sector 46.

1500 and 3000 K. The possible contributions of reflected light and thermal emission given the occultation depths in the TESS bandpass are shown in Fig. 4. In each panel, the curve is the contour for the measured occultation depth for a corresponding sector. The brightness temperature represents the thermal emission, while the geometric albedo represents the reflected light (Demory et al. 2011b). The geometric albedo and brightness temperature estimates are biased because the baseline planet flux is unknown, given that it varies. If we assume that the 4.5 μm *Spitzer* measurements can be extrapolated to the TESS wavelengths and if we adopt the maximum hemisphere-averaged temperature of 2697 K derived by Demory et al. (2016), we infer an upper limit of 0.379 for the geometric albedo.

4. Discussion

From our analysis we draw several conclusions. First, the transit depth across sectors is consistent within the uncertainties. Second, from the combined observations, we measured an occultation depth of 8 ± 2.5 ppm. And finally, the occultation varies from sector to sector, from 1.6σ to 3.4σ significance.

To study how significant our results are, we compared our models by measuring the relative likelihood to describe the observations while penalizing the number of parameters with the LOO cross-validation statistic, as done in Morris et al. (2021). In general, the preferred model is ranked first with a ΔLOO of zero. A more significant preference for a model relative to another yields a higher ΔLOO (Vehtari et al. 2015, 2016). The weight of a model can be interpreted as its probability of performing the best with future data among the considered models (Yao et al. 2018).

The results are summarised in Table 2. The varying occultation model is preferred followed by the combined occultation

Table 2. Difference in LOO cross-validation and weight between our model fitting an individual occultation per sector (labelled 'Occultation per sector'), a composite model of an occultation for all observations together ('Combined occultation'), and a model with no occultation ('No occultation').

Model	Rank	Δ LOO	Weight
Occultation per sector	1	0	0.639
Combined occultation	2	2.61	0.287
No occultation	3	11.38	0.074

model. The model with no occultation is ranked last. The models including an occultation as a parameter have a combined weight of 0.926, which strengthens the evidence of a positive detection. Moreover, the model with an occultation parameter for each sector takes most of the weight, being the one with more chances to perform best on future observations. From our MCMC best-fit and model comparison, we conclude that given the TESS observations, the occultation is detected and slightly favours a variable depth.

To get a better sense of the occultation variability, we used our MCMC algorithm to estimate the depth for each individual occultation. We discarded observations of partial occultations given the small number of measurements. The result is shown in Fig. 5. Negative depths have no physical meaning. The power spectrum on the results do not show a strong periodicity.

Considering the evidence provided in this study alone, the process responsible for a change in occultation depth remains unknown. If the change in occultation is of astrophysical origin, the planet undergoes a process that interchangeably obscures and brightens either its surface or the close vicinity of the planet. It
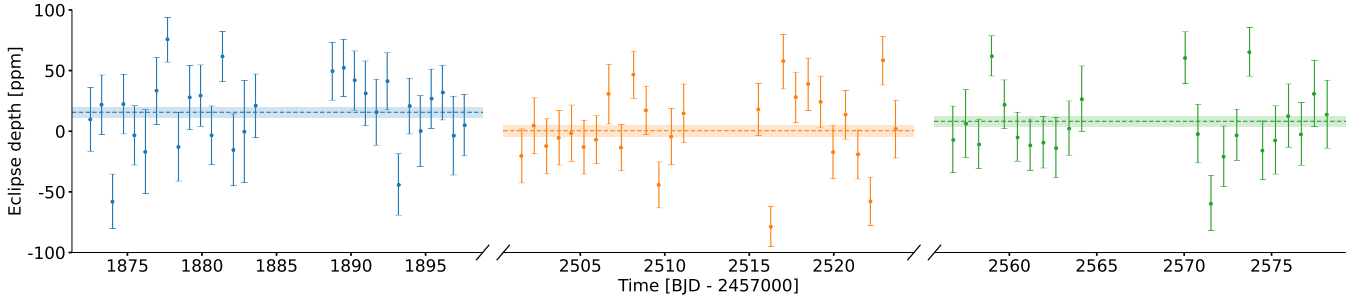
Fig. 5. Individual occultation of depth versus time. Partial occultations were discarded. Blue circles correspond to the best-fit median value in sector 21, orange circles belong to measurements in sector 44, and green circles correspond to sector 46. The error bars represent 1σ uncertainty. Horizontal dashed lines and the shaded area are the best-fit median value and 1σ uncertainty obtained by fitting over the entire sector (see Table 1).
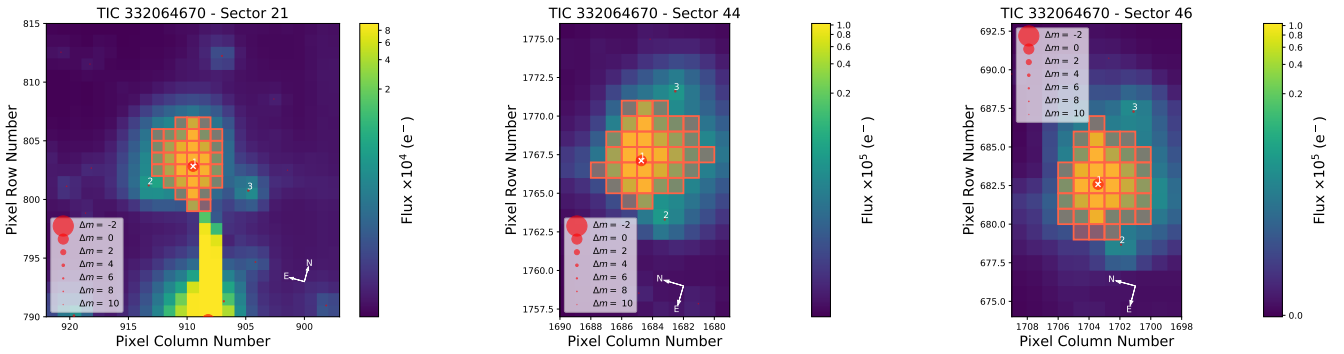

Fig. 6. Target pixel file (TPF) images for 55 Cnc, from TESS sectors 21 (*left*), 44 (*centre*), and 46 (*right*). The apertures used for light curve generation are over-plotted in red contour lines; sources identified in *Gaia* DR2 are also included with symbols correlated to their brightness compared to the target. Star number 2 is the companion, 55 Cnc B, while the much brighter 53 Cnc is seen at the bottom of the image for sector 21. Star number 3 can be found in the *Gaia* EDR3 (Gaia Collaboration 2016, 2021) under the ID 704966693493530496. These images were produced using `tpfplotter` (Aller et al. 2020).

is possible that TESS observed the system at different levels of activity (e.g. volcanism) in each sector. As mentioned in Sect. 1 the variability could be of stellar origin, an effect of star-planet interaction, catastrophic disintegration, a change in opacity due to volcanic activity, as a result of the presence of an inhomogeneous circumstellar torus of dust, or another unidentified process.

Given planet e's extremely short period, it is natural to compare it with other ultra-short period (USP) planets. Due to the strong stellar irradiation, Mercury-size planets can evaporate and lead to disintegration (Rappaport et al. 2012). However, based on our evidence we rule out an asymmetric transit shape (see Fig. 1), characteristic of a disintegrating planet due to a tail (and possibly leading a trail) of material, such as the case of KIC 12557548. Moreover, the residuals do not exhibit an excess or depression of light relative to the mean out-of-transit flux shortly before ingress or after egress. Since our measurements point towards a constant transit depth but a variable occultation depth, it is possible that the planet or its vicinity is covered by a variable amount of material with significant back-scattering and little forward scattering (Sanchis-Ojeda et al. 2015).

Variable contamination across different sectors could change the detected occultation depth, and we note that the orientation of the spacecraft was different in sector 21 than the latter two sectors. Inspecting the Target Pixel Files (TPF) (see Fig. 6) reveals that the contamination by 53 Cnc is minimal in the latter two sectors, and it may affect sector 21. However, the occultation depth in sector 21 is the largest, and contamination would bias the occultation towards shallower depths, so we infer that

removing the contamination would only strengthen the detection in sector 21.

As validation of our derived uncertainties in the occultation depth, we performed injection tests, which consist in injecting mock transits and occultations in the light curve residuals. We constructed the synthetic light curve with `batman` (Kreidberg 2015). The time at mid-transit was chosen randomly between $[t_0 + T_{14}/2, t_0 + (P - T_{14})/2]$ (somewhere between the end of true transit and the start of occultation), where t_0 is 55 Cnc e's mid-transit time, T_{14} its transit duration, and P its period. Based on the thermal contribution computed in Sect. 3.3, we chose to inject an occultation of 10 ppm in our residuals. Then we repeated the same exercise, but in a randomly drawn mid-transit time between $[t_0 + (P + T_{14})/2, t_0 + P - T_{14}/2]$ (between the end of true occultation and the start of transit).

The same MCMC algorithm as described in Sect. 2 is used on the data for one sector at a time. For each sector individually, we find a mid-transit time and occultation depth agreeing with the corresponding true values within 1σ. The uncertainties seem to be comparable to our results in Sect. 3, but in general tend to over or underestimate, pointing at correlated noise still present in the light curve.

5. Conclusions

At the present stage, we know that the planet exhibits a phase modulation too large to be attributed to reflected light and thermal emission (Winn et al. 2011; Sulis et al. 2019) and undergoes a significant change in day-side brightness temperature over time

(Demory et al. 2015; Tamburo et al. 2018). So far, the variability in the occultation depth has only been observed in the IR. Here we confirm the detection of the occultation on the combined TESS observations and present weak evidence of a variable occultation in the optical. The process causing these phenomena is still unknown. Based on our results, the possible contribution of reflected light in the measured signal puts an upper limit of 0.4 on the geometric albedo.

The exquisite precision demonstrated in CHEOPS observing this system (Morris et al. 2021) and the much anticipated *James Webb* Space Telescope (JWST) will most likely provide exciting findings about this enigmatic system. In particular, two proposals to observe 55 Cnc e in Cycle 1 were accepted. One programme aims to identify if the origin of the variable occultation depth is due to a 3:2 spin-orbit resonance (Brandeker et al. 2021), resulting in a different side of the planet being visible. The second project focusses on atmospheric characterisation by measuring the thermal emission spectrum from 3.8–12 micron (Hu et al. 2021). Furthermore, the planet K2-141b, a so-called lava world which has similar characteristics to 55 Cnc e, will also be observed by JWST (Dang et al. 2021). In the coming months, we might not only learn more about 55 Cnc e's nature, but about the USP population in general.

References

Agol, E., Luger, R., & Foreman-Mackey, D. 2020, AJ, 159, 123
Aller, A., Lillo-Box, J., Jones, D., Miranda, L. F., & Barceló Forteza, S. 2020, A&A, 635, A128
Astropy Collaboration (Robitaille, T. P., et al.) 2013, A&A, 558, A33
Astropy Collaboration (Price-Whelan, A. M., et al.) 2018, AJ, 156, 123
Beatty, T. G., Wong, I., Fetherolf, T., et al. 2020, AJ, 160, 211
Bourrier, V., Dumusque, X., Dorn, C., et al. 2018a, A&A, 619, A1
Bourrier, V., Ehrenreich, D., des Etangs, A. L., et al. 2018b, A&A, 615, A117
Brandeker, A., Alibert, Y., Bourrier, V., et al. 2021, JWST Proposal. Cycle 1, ID. #2084
Castelli, F., & Kurucz, R. L. 2004, Proceedings of the International Astronomical Union, IAU Symp. 210, Modelling of Stellar Atmospheres, eds. N. Piskunov et al. 2003, poster A20
Claret, A. 2017, A&A, 600, A30
Dang, L., Cowan, N. B., Hammond, M., et al. 2021, JWST Proposal. Cycle 1, ID. #2347
Dawson, R. I., & Fabrycky, D. C. 2010, ApJ, 722, 937
Demory, B.-O., Gillon, M., Deming, D., et al. 2011a, A&A, 533, A114
Demory, B.-O., Seager, S., Madhusudhan, N., et al. 2011b, ApJ, 735, L12
Demory, B.-O., Gillon, M., Madhusudhan, N., & Queloz, D. 2015, MNRAS, 455, 2018
Demory, B.-O., Gillon, M., de Wit, J., et al. 2016, Nature, 532, 207
Dragomir, D., Matthews, J. M., Winn, J. N., & J. F. R. 2012, Proc. Int. Astron. Union, 8, 52
Ehrenreich, D., Bourrier, V., Bonfils, X., et al. 2012, A&A, 547, A18
Fazio, G. G., Hora, J. L., Allen, L. E., et al. 2004, ApJS, 154, 10
Folsom, C., Fionnagáin, D. Ó, Fossati, L., et al. 2020, A&A, 633, A48
Foreman-Mackey, D. 2016, J. Open Source Softw., 1, 24
Foreman-Mackey, D., Savel, A., Luger, R., et al. 2021, https://doi.org/10.5281/zenodo.4737444
Gaia Collaboration (Prusti, T., et al.) 2016, A&A, 595, A1
Gaia Collaboration (Brown, A. G. A., et al.) 2021, A&A, 649, A1
Garhart, E., Deming, D., Mandell, A., et al. 2020, AJ, 159, 137
Gelman, A., & Rubin, D. B. 1992, Stat. Sci., 7, 457
Ginsburg, A., Sipőcz, B. M., Brasseur, C. E., et al. 2019, AJ, 157, 98
Harris, C. R., Millman, K. J., van der Walt, S. J., et al. 2020, Nature, 585, 357
Heller, R. 2019, A&A, 623, A137
Hippke, M., David, T. J., Mulders, G. D., & Heller, R. 2019, AJ, 158, 143
Hu, R., Brandeker, A., Damiano, M., et al. 2021, JWST Proposal. Cycle 1, ID. #1952
Hunter, J. D. 2007, Comput. Sci. Eng., 9, 90
Husser, T.-O., von Berg, S. W., Dreizler, S., et al. 2013, A&A, 553, A6
Jenkins, J. M., Twicken, J. D., McCauliff, S., et al. 2016, SPIE, 9913, 1232
Kipping, D. M. 2013, MNRAS, 435, 2152
Kipping, D., & Jansen, T. 2020, Res. Notes Am. Astron. Soc., 4, 170
Kreidberg, L. 2015, PASP, 127, 1161
Kumar, R., Carroll, C., Hartikainen, A., & Martin, O. A. 2019, J. Open Source Softw., 4, 1143
Lightkurve Collaboration (Cardoso, J. V., et al.) 2018, Astrophysics Source Code Library [record ascl:1812.013]
Luger, R., Agol, E., Foreman-Mackey, D., et al. 2019, AJ, 157, 64
Mallonn, M., Köhler, J., Alexoudi, X., et al. 2019, A&A, 624, A62
Mandel, K., & Agol, E. 2002, ApJ, 580, L171
McArthur, B. E., Endl, M., Cochran, W. D., et al. 2004, ApJ, 614, L81
Morris, B. M., Delrez, L., Brandeker, A., et al. 2021, A&A, 653, A173
Rappaport, S., Levine, A., Chiang, E., et al. 2012, ApJ, 752, 1
Ricker, G. R., Winn, J. N., Vanderspek, R., et al. 2014, J. Astron. Teles. Instrum Syst., 1, 1
Salvatier, J., Wiecki, T. V., & Fonnesbeck, C. 2016, PeerJ Comput. Sci., 2, e55
Sanchis-Ojeda, R., Rappaport, S., Pallè, E., et al. 2015, ApJ, 812, 112
Sulis, S., Dragomir, D., Lendl, M., et al. 2019, A&A, 631, A129
Tamburo, P., Mandell, A., Deming, D., & Garhart, E. 2018, AJ, 155, 5
Theano Development Team. (Al-Rfou, R., et al.) 2016, ArXiv e-prints [arXiv:1605.02688]
VanderPlas, J. T. 2018, ApJS, 236, 16
Vehtari, A., Simpson, D., Gelman, A., Yao, Y., & Gabry, J. 2015, ArXiv e-prints [arXiv:1507.02646]
Vehtari, A., Gelman, A., & Gabry, J. 2016, Stat. Comput., 27, 1413
Virtanen, P., Gommers, R., Oliphant, T. E., et al. 2020, Nat. Methods, 17, 261
von Braun, K., Boyajian, T. S., ten Brummelaar, T. A., et al. 2011, ApJ, 740, 49
Werner, M. W., Roellig, T. L., Low, F. J., et al. 2004, ApJS, 154, 1
Winn, J. N., Matthews, J. M., Dawson, R. I., et al. 2011, ApJ, 737, L18
Yao, Y., Vehtari, A., Simpson, D., & Gelman, A. 2018, Bayesian Anal., 13, 917

Appendix A: Posterior distributions

For completeness, we present the corner plot of the parameters sampled from the transit model MCMC fit in Fig. A.1, while Fig. A.2 presents some parameters sampled from the occultation model MCMC fit.

Appendix B: RMS versus bin size

If the remaining noise in the observations is white, the residual RMS should decrease as $1/\sqrt{n}$, where n is the size of the bin. The resulting plots of our occultation model residuals are shown in Fig. B.1.
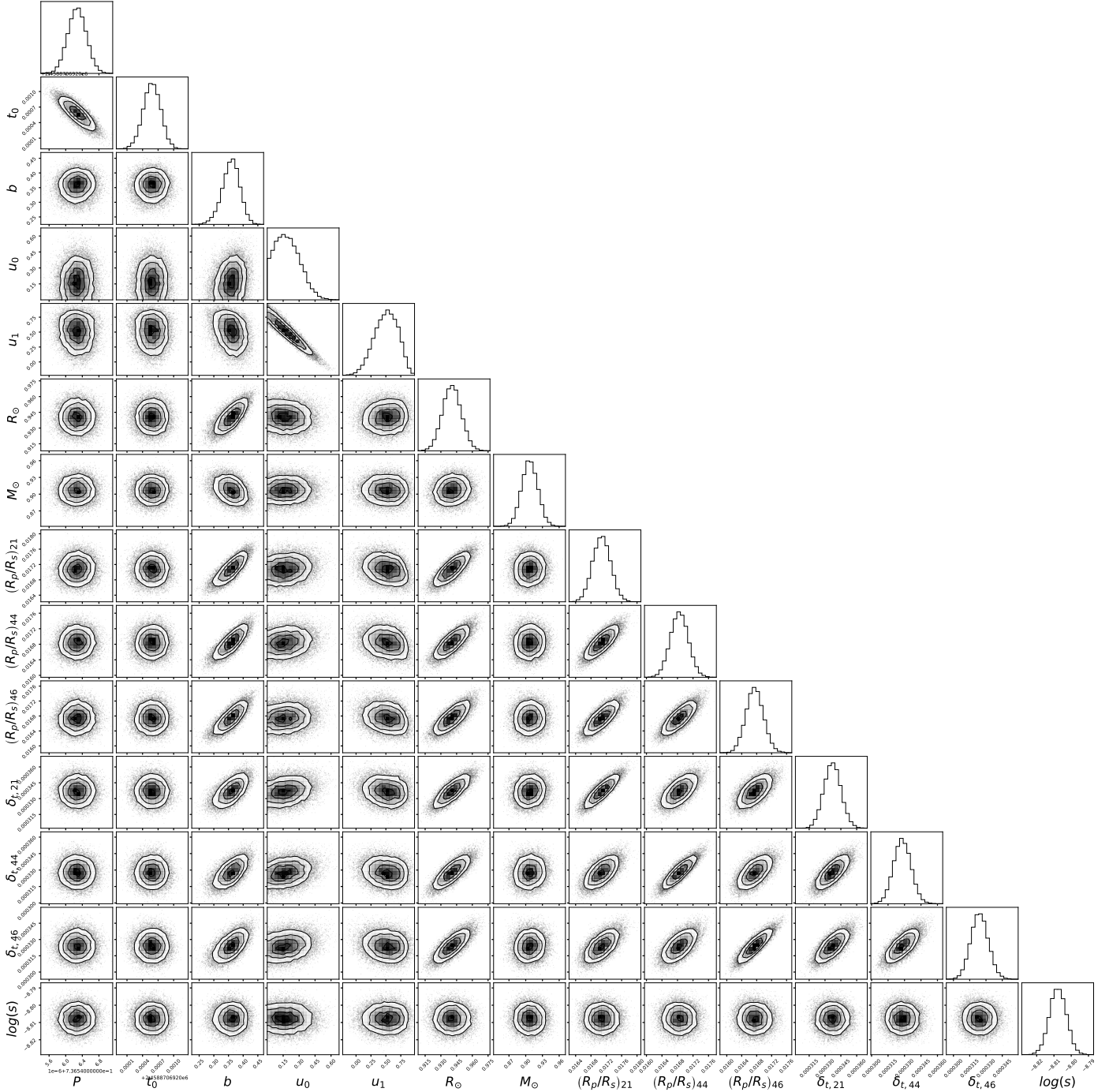
Fig. A.1: Posterior distributions and joint correlations between all free parameters in the transit model fit. The parameters are: orbital period P, mid-transit time t_0, impact parameter b, quadratic limb-darkening coefficients u_0 and u_1, stellar radius $R_\odot$ and mass $M_\odot$, planet-to-star radius ratio R_p/R_s, and transit depth δ_t with a numeric subscript corresponding to the sector. We note that $log(s)$ is the natural logarithm of the flux uncertainty for each measurement.
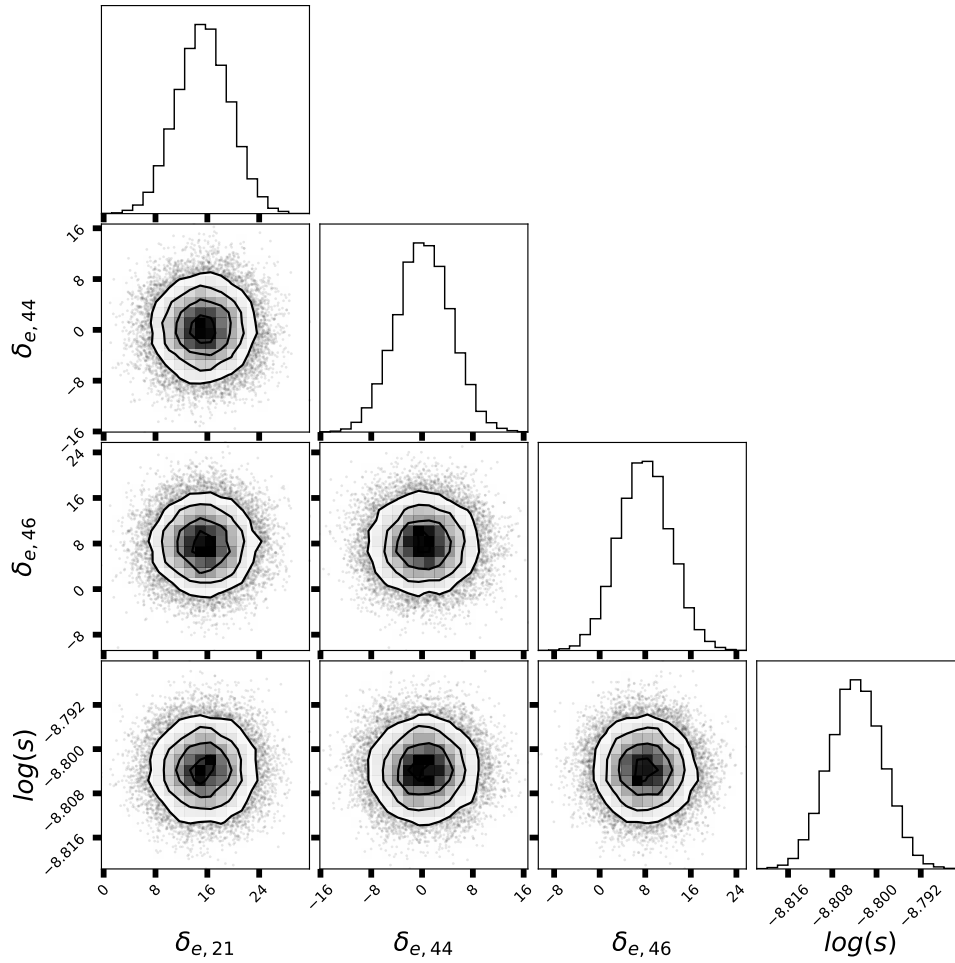
Fig. A.2: Posterior distributions and joint correlations between all free parameters in the occultation model fit. The parameters shown are: occultation depth δ_t with a numeric subscript corresponding to the sector. Furthermore, $log(s)$ is the natural logarithm of the flux uncertainty for each measurement.
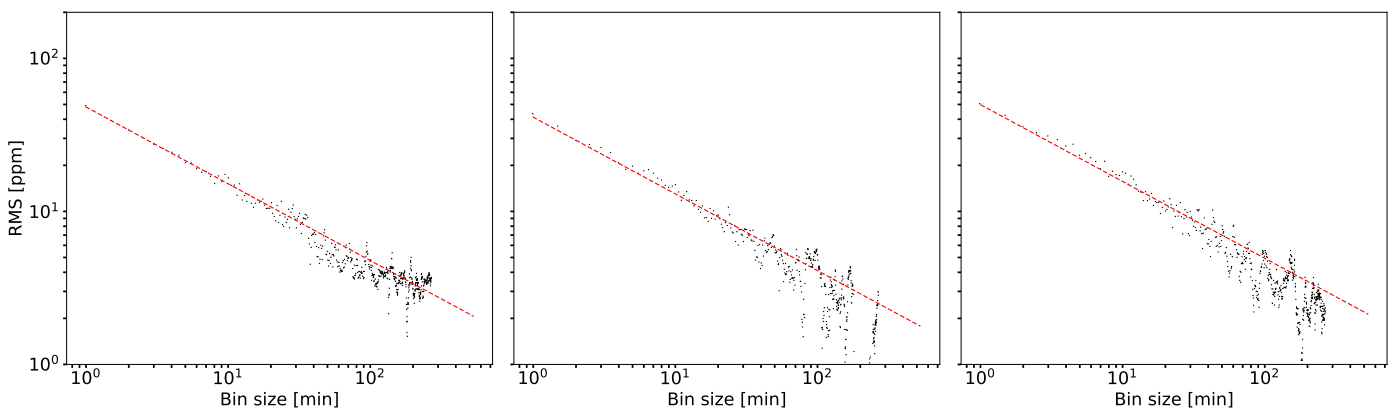

Fig. B.1: Photometric residual RMS for different bin size in minutes for sector 21 (left), sector 44 (middle), and sector 46 (right). The red-dashed line shows the expected decrease in Poisson noise precision normalised to a 2-min bin.